catalysts

MDPI

Article

Guaiacol to Aromatics: Efficient Transformation over In Situ-Generated Molybdenum and Tungsten Oxides

Mariyam Mukhtarova, Maria Golubeva *, Alexey Sadovnikov and Anton Maximov *

A.V. Topchiev Institute of Petrochemical Synthesis, Russian Academy of Sciences (TIPS RAS), Moscow 119991, Russia

* Correspondence: vinnikova@ips.ac.ru (M.G.); max@ips.ac.ru (A.M.)

Abstract: The development of catalysts for the hydrodeoxygenation of bio-based feedstocks is an important step towards the production of fuels and chemicals from biomass. This paper describes in situ-generated bulk molybdenum and tungsten oxides in the hydrodeoxygenation of the lignin-derived compound guaiacol. The catalysts obtained were studied using powder X-ray diffraction, X-ray photoelectron spectroscopy, scanning electron microscopy, high-resolution transition electron microscopy, diffuse reflectance infrared Fourier transform spectroscopy, and Raman spectroscopy. The use of metal carbonyls as precursors was shown to promote the formation of amorphous molybdenum oxide and crystalline tungsten phosphide under hydrodeoxygenation conditions. The catalysts' activity was investigated under various reaction conditions (temperature, H_2 pressure, solvent). MoO_x was more active in the partial and full hydrodeoxygenation of guaiacol at temperatures of 200–380 °C (5 MPa H_2, 6 h). However, cyclohexane, which is an undesirable product, was formed in significant amounts using MoO_x (5 MPa H_2, 6 h), while WO_x was more selective to aromatics. When using dodecane as a solvent (380 °C, 5 MPa H_2, 6 h), the benzene-toluene-xylenes fraction was obtained with a 96% yield over the WO_x catalyst.

Keywords: MoO_x; WO_x; guaiacol; hydrodeoxygenation; vacancy sites; dispersed catalysts; transition metal oxides; aromatic hydrocarbons; BTX

Citation: Mukhtarova, M.; Golubeva, M.; Sadovnikov, A.; Maximov, A. Guaiacol to Aromatics: Efficient Transformation over In Situ-Generated Molybdenum and Tungsten Oxides. *Catalysts* **2023**, *13*, 263. https://doi.org/10.3390/catal13020263

Academic Editors: Linda Zh Nikoshvili, Lioubov Kiwi-Minsker and Valentin Yu Doluda

Received: 25 December 2022
Revised: 13 January 2023
Accepted: 17 January 2023
Published: 23 January 2023

1. Introduction

Lignocellulosic biomass is a promising and widespread source of renewable energy [1,2]. One of the components of lignocellulosic biomass is lignin, which consists of oxygen-containing derivatives of phenylpropane. The structure of lignin allows it to be used as a source for the production of phenols and various aromatic compounds [3].

The main method for the processing of low-molecular-weight lignin derivatives is catalytic hydrodeoxygenation (HDO). Supported noble metals are actively involved in the HDO of different oxygenated compounds and show high catalytic activity. Nevertheless, the high cost of noble metals is a significant disadvantage in their application [4]. Transition metal phosphides, carbides, and nitrides are reported to be potential candidates to replace expensive catalysts (Table 1) [4].

Table 1. Some results from the literature of the lignin-derived compound HDO over Mo- and W-containing catalysts.

Catalyst	Feedstock	Reaction Conditions [a]	Conversion, %	Selectivity, %	Ref.
Mo_xC/CNF	0.68 g cinnamaldehyde in 50 mL toluene	200 °C, 2 MPa H_2, ~2.75 h [a]	90	40.9 for hydrocinnamaldehyde 25.8 for β-methylstyrene	[5]
W_xC/CNF		200 °C, 2 MPa H_2, ~5.75 h [a]	90	43 for hydrocinnamaldehyde 34 for β-methylstyrene	
Pd/α-MoC	anisole	200 °C [b]	21.5	94 for benzene	[6]
Mo_2C@ BMZIF-700 °C (4 h)	0.12 g guaiacol in 20 mL n-decane	330 °C, 4 MPa H_2, 4 h [a]	97	70 for phenol	[7]
Mo_2N@ NC500/SBA-15	3 wt. % guaiacol in n-decane	380 °C, 2 MPa H_2 [c]	100	92 to benzene + toluene	[8]
in situ formed MoP	10 wt. % guaiacol in n-dodecane	360 °C, 5 MPa H_2, 6 h [a]	90	80 for phenol	[9]
in situ formed WP		340 °C, 5 MPa H_2, 1 h [a]	53	78 for phenol	
MoP		340 °C, 5 MPa H_2, 6 h [a]	90	66 for phenol	[10]
WP		380 °C, 5 MPa H_2, 6 h [a]	89	84 for phenol	
in situ formed MoO_x		380 °C, 1 MPa H_2, 6 h [a]	100	89 for BTX	This work
in situ formed WO_x		380 °C, 5 MPa H_2, 6 h [a]	100	96 for BTX	

[a] a batch reactor was used; [b] a fixed bed quartz tubular reactor was used; [c] a micro-hydrogenation reactor was used.

However, the activity of such catalysts is partially related to the presence of oxygen on their surface, including in the metal oxide form. Therefore, transition metal oxides can also be considered as alternative HDO catalysts. Oxygen vacancies (coordinatively unsaturated metal sites) in oxides are reported to be active sites in HDO reactions [11,12]. Vacancies are formed as a result of H_2 adsorption on the oxide surface and the subsequent removal of oxygen as a part of water [13]. The electron-lone-pair oxygen in a substrate is adsorbed on the active site which leads to HDO as a result of the cleavage of the C–O bond [11].

Mo- and W-containing compounds are well-known in the field of catalysis. It has been reported that Mo and W are resistant to oxygen, acids, and alkalis and, therefore, they are used for oxygen removal [14]. Efficient hydrodeoxygenation of various substrates over molybdenum oxides have been previously reported in a number of works [11,13], while pure tungsten oxides have not provided high selectivity for hydrodeoxygenation products [15]. Prasomsri et al. found that MoO_3 can be used for the effective HDO of linear and cyclic ketones, phenolics, and cyclic ethers at 250–400 °C under low H_2 pressure with the formation of olefins and aromatics [13]. Selectivity for hydrocarbons was reportedly more than 97% at 400 °C. Zhang et al. carried out the HDO of guaiacol, o-cresol, eugenol, trans-anethole, vanillin, and diphenyl ether over MoO_3 under mixed H_2 + N_2 pressure at 300–360 °C [11]. Aromatics were obtained with the selectivity of 45.3–93.8% at 340 °C. Whiffen et al. tested MoO_3 and MoO_2 in the HDO of p-cresol at 325–375 °C, under 4.14–4.83 MPa H_2 in a batch reactor [16]. Toluene was the main reaction product over both catalysts. MoO_2 was noted to be more active in the HDO than MoO_3. Several studies were devoted to m-cresol HDO to toluene over WO_x promoted by other metals [17–19]. Wang et al. demonstrated that Pt-WO_x/C catalyst can convert m-cresol into toluene with 94% selectivity (350 °C, 0.1 MPa H_2, H_2 flow rate: 12 mL/min, WHSV = 60 h^{-1}) [17]. In another work, they used n-hexane which produced H_2 by dehydration [18]. Direct bonding of Pt and WO_x contributed to oxide stabilization and oxygen vacancies formation, which are responsible for direct hydrogenolysis of the C–O bond in m-cresol [17]. Chen et al. reported similar regularities using a Ni-WO_x/C catalyst [19]. Toluene was obtained from m-cresol with 89% selectivity at 350 °C, under 0.1 MPa H_2, WHSV of 1 h^{-1}.

Previously, the in situ formation of transition metal catalysts during hydroprocessing of various model compounds and real feedstocks were studied [9,20–24]. In our recent works, the in situ formation of phosphide catalysts, including molybdenum and tungsten phosphides in the HDO of guaiacol, was investigated for the first time [9,20,21]. The

absence of a catalyst synthesis stage, and therefore a simplification of the process, is one of the advantages of catalyst in situ formation. The use of metal carbonyls in combination with an oil-soluble phosphorus precursor made it possible to obtain the corresponding phosphides. It was found that, in addition to phosphides, the catalyst surface also contains metal oxides.

In the present work, molybdenum and tungsten oxides were obtained in situ from carbonyls during the HDO of guaiacol (a low-molecular-weight lignin derivative) and investigated in this process for the first time. We report that these bulk catalysts are highly active in the HDO of guaiacol to aromatics, in particular, to a benzene-toluene-xylenes (BTX) fraction. MoO_x converted guaiacol into BTX with the highest selectivity of 89% (380 °C, 1 MPa H_2, 6 h) at full conversion, while using WO_x the highest selectivity for BTX was 96% (380 °C, 5 MPa H_2, 6 h). In comparison with oxides obtained in the present work, phosphides and carbides promoted the obtaining of phenol as a main reaction product of guaiacol conversion (Table 1). In situ-generated MoP and WP from the same metal precursors in the HDO of guaiacol allows the obtaining of phenol as a main reaction product [9]. The highest phenol selectivity rates were 80% and 78% using MoP and WP, respectively. Ex situ-generated bulk MoP and WP also made a contribution to the phenol obtained from guaiacol (with 66% and 84% selectivity over MoP and WP, respectively) [10]. Kurisingal et al. made a report about selective guaiacol HDO to phenol using bimetallic Zn-Co zeolitic imidazolate framework (BMZIF)-decorated molybdenum carbide [7]. The distribution of active species, such as Mo_2C, MoO_3, ZnO, and CoO was found to have a high influence on guaiacol conversion and phenol selectivity. The most active Mo_2C@BMZIF- 700 °C (4 h) catalyst promoted a 97% guaiacol conversion and 70% phenol selectivity. Wang et al. demonstrated that an SBA-15-supported ultrastable Mo_2N@CN catalyst showed similar catalytic activity in the guaiacol HDO to the catalysts reported in the present work [8]. A benzene and toluene mixture was obtained with 92% selectivity at 380 °C, while at 320 °C phenol was the main product. However, the synthesis of nitrides is a laborious procedure, while we report an easy method for catalyst synthesis.

2. Results and Discussion

2.1. Catalyst Characterization

In the present work, thein situ-formation of molybdenum and tungsten oxides from molybdenum and tungsten carbonyls during guaiacol hydrodeoxygenation was investigated. Metal carbonyl complexes are known to react with water, other sources of OH-groups, and oxygen with the formation of oxides [25–31]. A substrate used in this work has an OH-group, and the HDO process involves the formation of water. The catalysts obtained were called MoO_x and WO_x, and were studied using powder X-ray diffraction (XRD), X-ray photoelectron spectroscopy (XPS), high-resolution transmission electron microscopy (HRTEM) with energy-dispersive X-ray spectroscopy (EDX), scanning electron microscopy (SEM), diffuse reflectance infrared Fourier transform spectroscopy (DRIFTS), and Raman spectroscopy.

The XRD patterns of catalyst precursors are shown in Figure S1 and correspond to crystalline $Mo(CO)_6$ (PDF №75-1336) and $W(CO)_6$ (PDF № 84-2314). Figure 1a shows the XRD of MoO_x obtained at temperatures of 120–360 °C. MoO_x is shown to be amorphous over the whole temperature range. The evolution of the WO_x catalyst with temperature can be followed using XRD (Figure 1b). At 120 °C the WO_x diffractogram has characteristic peaks at 15.52° and 16.68°, which are assigned to $W(CO)_6$. When temperature rises to 180 °C, carbonyl partially decomposes with the formation of a WO_3 phase (PDF № 5-363), of which characteristic peaks are observed at 70.64° and 72.88°. With a further increase in temperature, the peaks related to carbonyl disappear, which characterizes its complete decomposition and oxidation. In addition, at 240 °C, WO_3 is converted to $W_{18}O_{49}$ (PDF № 71-2450). This phase was identified in the sample obtained at 240–360 °C. The characteristic peaks at 23.52° and 48.12° correspond to the (010) and (020) planes in $W_{18}O_{49}$ [32]. The average crystallite sizes of $W_{18}O_{49}$ were 2.0 ± 0.6 nm, 13.3 ± 0.9 nm and 14.6 ± 0.1 nm at

240, 300, and 360 °C, respectively. Therefore, a temperature increase affects the growth of $W_{18}O_{49}$ crystallites. Thus, the XRD of WO_x catalyst shows $W(CO)_6$ decomposition with the formation of WO_3 at 180 °C, and further WO_3 reduction at 240 °C to $W_{18}O_{49}$.

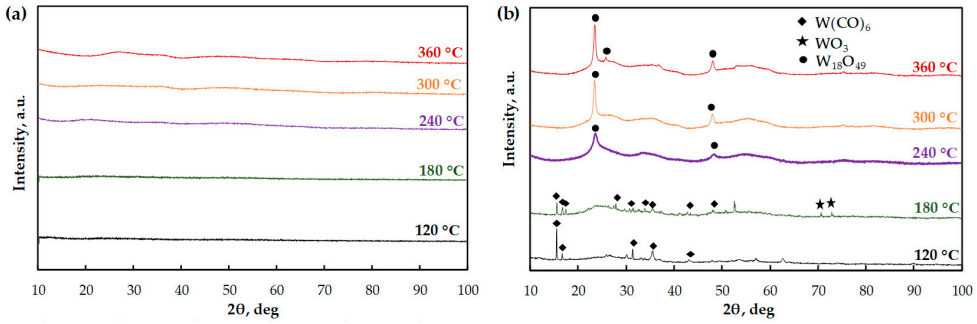

Figure 1. Powder X-ray diffraction of (**a**) MoO_x, (**b**) WO_x formed in situ during guaiacol HDO (10 wt. % solution in toluene). Reaction conditions: 120–360 °C, 5 MPa H_2, 6 h.

To identify electronic states on the surface of the catalysts, the XPS technique was applied. For MoO_x obtained at 120 °C (Figure 2a), the doublet at 232.5 ($3d_{5/2}$) and 235.7 ($3d_{3/2}$) eV in the Mo 3d region can be assigned to Mo^{6+} in MoO_3 [33]. The peaks at 231.8 ($3d_{5/2}$) and 234.8 ($3d_{3/2}$) eV are ascribed to Mo^{5+} [34]. The presence of Mo^{5+} species indicates the existence of the oxygen vacancies in MoO_3 [35,36]. Choi and Thompson noted that the reduction of Mo^{6+} to Mo^{4+} can proceed through a +5 intermediate oxidation state [37]. Figure 2b shows the XP-spectrum of WO_x in the W 4f region. The peaks with binding energies of 34.7 ($4f_{7/2}$) and 35.6 ($4f_{5/2}$) eV correspond to W^{4+} in WO_2 [38]. The other two peaks observed at 35.9 ($4f_{7/2}$) and 38.0 ($4f_{5/2}$) eV are attributed to W^{6+} in WO_3 [39].

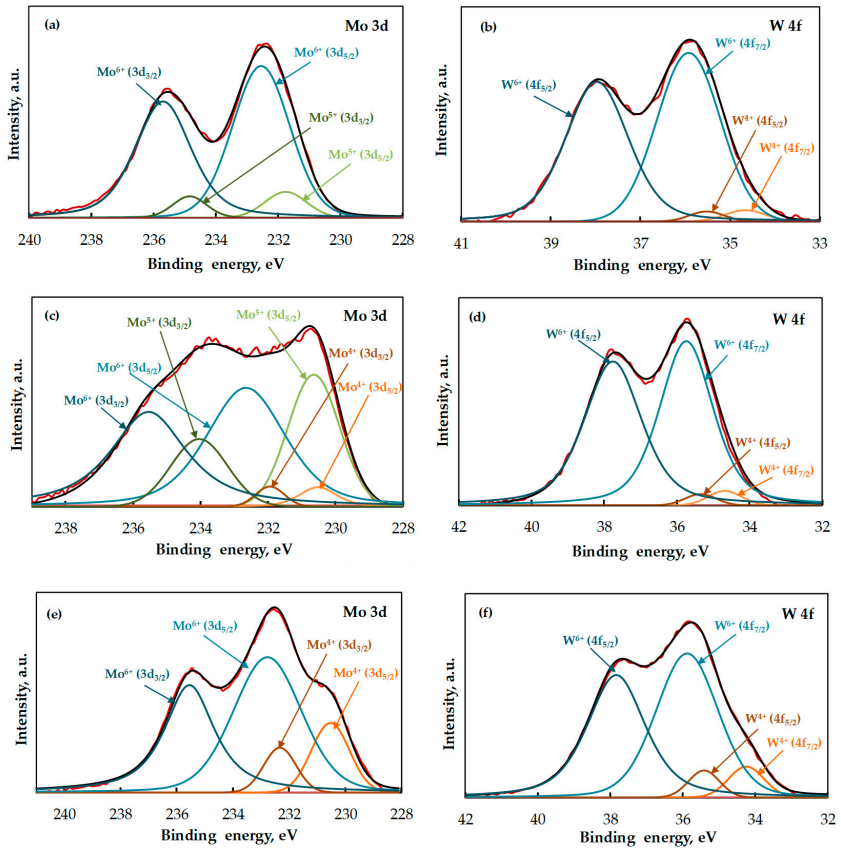

Figure 2. X-ray photoelectron spectroscopy of MoO_x and WO_x catalysts formed in situ during guaiacol HDO (10 wt. % solution in toluene) at (**a**,**b**) 120 °C, (**c**,**d**) 240 °C and (**e**,**f**) 360 °C.

The XP-spectrum of MoO_x obtained at 240 °C is presented in Figure 2c. The peaks located at 230.6 ($3d_{5/2}$) and 234.0 ($3d_{3/2}$) eV correspond to Mo^{5+} species [34]. The doublet at 232.7 ($3d_{5/2}$) and 235.5 ($3d_{3/2}$) eV is attributed to Mo^{6+} [33]. The doublet at 230.5 ($3d_{5/2}$) and 231.9 ($3d_{3/2}$) eV is assigned to Mo^{4+} in MoO_2 [33]. Therefore, with a temperature increase from 120 to 240 °C, Mo^{6+} and Mo^{5+} begin to reduce to Mo^{4+}. The XP-spectrum of WO_x obtained at 240 °C is presented in Figure 2d. The binding energies of 34.7 and 35.3 eV are defined as W^{4+} in the $4f_{7/2}$ and $4f_{5/2}$ regions, respectively. The doublet observed at 35.7 ($4f_{7/2}$) and 37.8 ($4f_{5/2}$) eV is attributed to W^{6+} in WO_3 [39].

The XP-spectrum of MoO_x (Figure 2e) obtained at 360 °C shows two peaks located at 230.5 ($3d_{5/2}$) and 232.3 ($3d_{3/2}$) eV and assigned to Mo^{4+} in MoO_2 [33]. The predominant doublet with peaks at 232.8 ($3d_{5/2}$) and 235.5 ($3d_{3/2}$) eV corresponds to Mo^{6+} in MoO_3 [33]. It is important to note that the presence of Mo^{5+} is not observed at 360 °C. Thus, at this temperature Mo^{5+} is completely reduced to Mo^{4+}. WO_x XP-spectrum (Figure 2f) shows the peaks with binding energies of 34.3 and 35.4 eV corresponding to W^{4+} in WO_2 in $4f_{7/2}$ and $4f_{5/2}$ regions, respectively [38]. The peaks observed at 35.9 ($4f_{7/2}$) and 37.8 ($4f_{5/2}$) eV are attributed to W^{6+} in WO_3 [39].

According to the XPS data, the total content of W^{4+} in the WO_x catalyst increases with a temperature rise from 240 to 360 °C, which is associated with the reduction of W^{6+} to W^{4+} (Table S1). In the case of MoO_x, Mo^{6+} and Mo^{5+} species are also reduced to Mo^{4+} with a temperature increase.

The XP-spectra in C 1 s and O 1 s regions of the catalysts obtained at various temperatures are shown in Figures S2 and S3. The same peaks are shown to be observed in the spectra of both catalysts. For example, there are two peaks located at 283.7 and 284.3 eV in the spectrum of MoO_x (C 1 s region) obtained at 120 °C (Figure S2). These peaks correspond to the C-C bond [40,41]. The other peaks observed at 285.2 and 288.8 eV can be assigned to the C-O and O = C-O bonds, respectively [42,43]. The presence of these peaks is associated with the adsorption of reaction products on the catalyst surface. In addition, the peaks corresponding to C-O can also be associated with the carbonyl groups in $Mo(CO)_6$ and $W(CO)_6$.

As shown in Figure S3, there are three peaks in the XP-spectra of MoO_x and WO_x (O 1 s region) obtained at 120 and 240 °C. In the case of MoO_x obtained at 120 °C, the binding energies of 530.5 and 531.7 eV are assigned to the Mo-O and Mo-OH bonds [44]. The XP-spectrum of WO_x obtained at 120 °C has two peaks at 530.7 and 532.0 eV, which can be attributed to W-O and W-OH, respectively [45]. Thus, at 120 and 240 °C, the presence of molybdenum and tungsten oxides and OH-groups on the surface of the catalysts is observed. The peaks located at 533.0 and 533.7 eV correspond to the C = O/C-OH bonds [41]. These peaks can be associated with the presence of water and oxygenated compounds on the surface of catalysts [46]. There are only two peaks corresponding to Me-O and Me-OH in XP-spectra of MoO_x and WO_x obtained at 360 °C. It can be concluded that at 360 °C carbonyls are completely converted into the corresponding molybdenum and tungsten oxides.

Figure 3 presents the SEM images of MoO_x and WO_x obtained at different reaction temperatures (120, 240, 360 °C). The MoO_x catalyst is represented by close-to-spherical particles of different sizes. The morphology of MoO_x (Figure 3a,c,e) is shown to not undergo significant changes with a temperature increase. The various morphology of the WO_x catalyst (Figure 3b,d,f) is observed at different temperatures. At 120 °C, the catalyst particles are close to spherical; at 240 °C, the particles do not have a definite morphology; at 360 °C, the particles are urchin-like spheres.

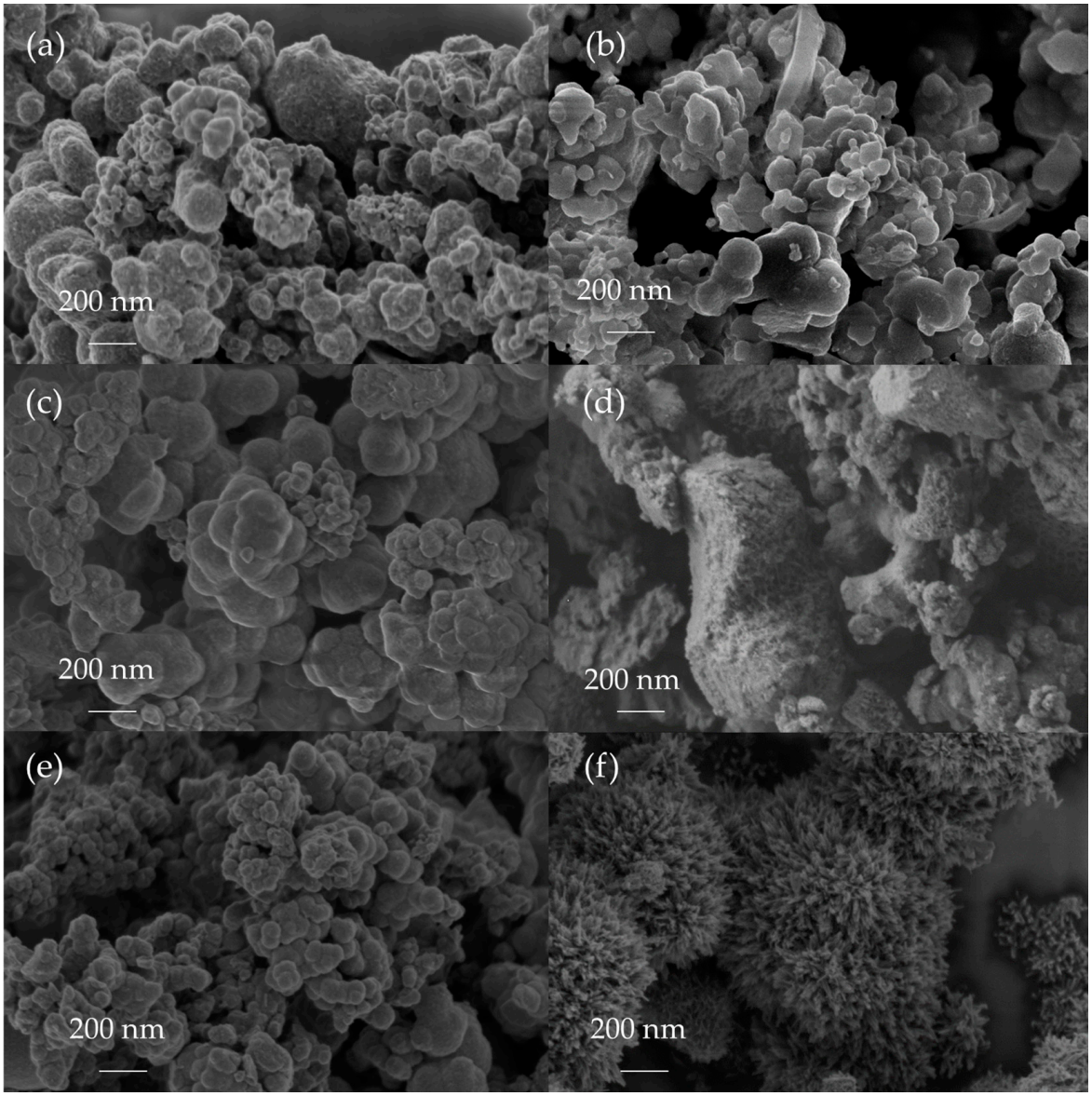

Figure 3. The SEM images of MoO_x and WO_x catalysts formed in situ during guaiacol HDO (10 wt. % solution in toluene) at (**a**,**b**) 120 °C, (**c**,**d**) 240 °C and (**e**,**f**) 360 °C.

HRTEM, DRIFTS and Raman spectroscopy was used to study catalysts formed at 360 °C. HRTEM was used to observe the morphology of the catalysts (Figure 4). As shown in Figure 4a, MoO_x represents agglomerates of particles. Moreover, the sample of MoO_x is amorphous (Figure 4b), which confirms the powder XRD results. Particle sizes are difficult to calculate due to agglomeration, since the edges of individual particles are not clearly visible. WO_x consists of urchin-like spheres, which are made up of nanorods with an average length of ~70–80 nm and width of ~8–10 nm (Figure 4c,d). According to the HRTEM, WO_x has a crystal lattice with the interplanar spacing of 0.38 nm, which corresponds to the (010) plane in $W_{18}O_{49}$ [47,48]. Figures S4 and S5 show the elemental maps of MoO_x and WO_x, respectively. Uniform distribution of metal and oxygen is observed for both samples. Energy-dispersive X-ray spectroscopy was used to study the elemental content of the catalysts. The ratio of O/Me calculated from the EDX spectra was ~1.5 for MoO_x and ~2.3 for WO_x (Figure S6).

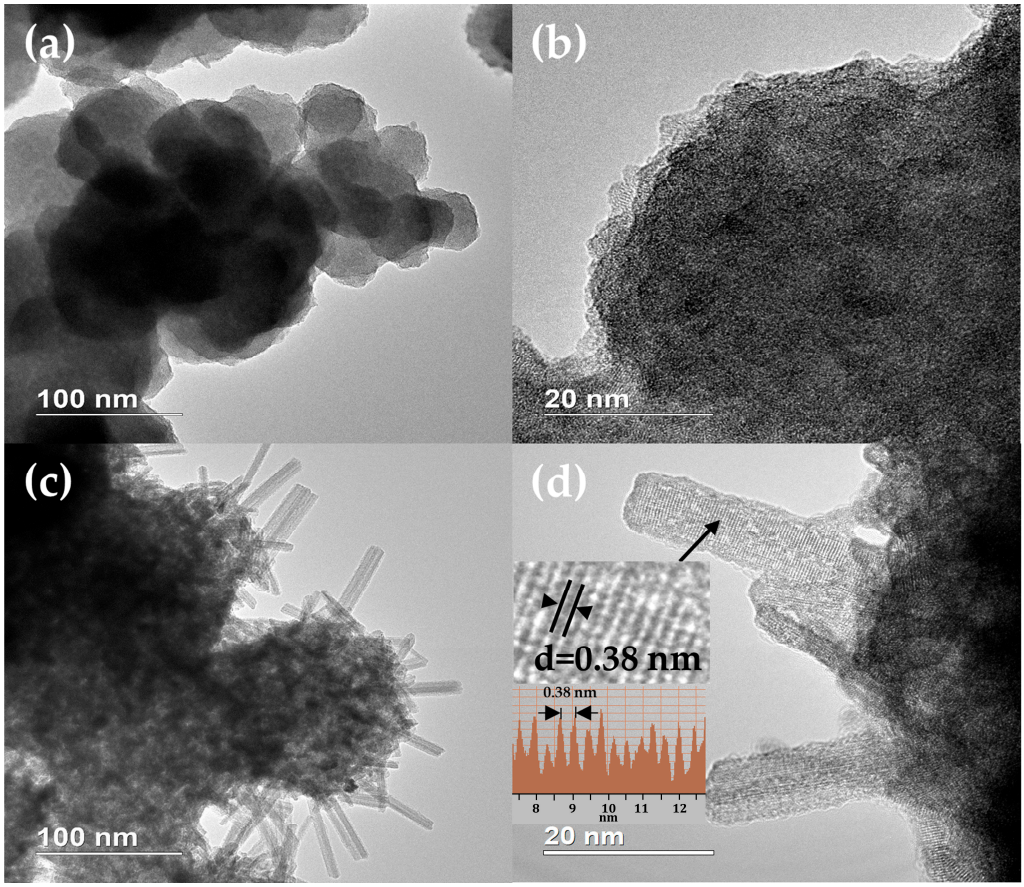

Figure 4. The microphotographs of the catalysts obtained in situ during guaiacol HDO (10 wt. % solution in toluene) (**a**,**b**) MoO_x, (**c**,**d**) WO_x.

The DRIFT spectra of MoO_x are shown in Figure S7. The intense bands of Me-O at 1000–900 cm^{-1} (at room temperature) are attributed to molybdenum oxide (Figure S7) [49]. There is also a broad band at 3400–3200 cm^{-1} from the stretching vibration, and at 1630 cm^{-1} from the bending vibration of OH-groups in the spectra. This is caused by the presence of water on the catalyst surface. The band growth from 3300 to 1630 cm^{-1} occurs due to water removal from a surface layer of the sample with an increase in temperature from 100 to 300 °C [50]. The presence of the bands at 3080 and 2950–2850 cm^{-1} is assigned to the C-H bonds of aryl and alkyl groups, respectively. In addition, the bands at 1392 cm^{-1} and 1425 cm^{-1} are attributed to the bending vibration of C-H bonds of the alkyl group. A further increase and decrease in temperature also shows the presence of aromatic compounds (the bands at 3080 and 1510 cm^{-1}) [51] and alkyl groups (the bands at 2950–2850 cm^{-1}) [52]. The band at 3740 cm^{-1} is attributed to the vibrations of OH-groups in reaction products.

The DRIFT spectra of WO_x are shown in Figure S8. The intense band at 990 cm^{-1} at a room temperature is attributed to the Me-O bond, which indicates the presence of tungsten oxide [52]. Water (the bands at 3300 and 1620 cm^{-1} from the stretching and bending vibrations of O-H, respectively) [50] and organic compounds are also present in small amounts (the bands at 3080 cm^{-1} from the bending vibrations of C-H in aromatic ring and at 1510 cm^{-1} from bending vibrations of aromatic ring) on the catalyst surface [51]. When the sample is calcined from room temperature to 300 °C, water is actively released from the sample layer to the surface, as evidenced by the growth of the bands at 3400 and 1620 cm^{-1}. The bands from the vibrations of the C-H bonds in aromatic compounds (3080 and 1510 cm^{-1}) and the C-H bonds in alkyl groups (CH_2, CH_3), and the bands at 2950–2850 cm^{-1} from stretching vibrations and 1460 cm^{-1} from bending vibrations also become more intense [53]. At 450 °C, the band at 3150 cm^{-1}, characteristic of condensed

aromatic rings, appears on the surface. The band at 3750 cm^{-1} exists over a whole temperature range and is attributed to OH-groups in different aromatic products of guaiacol HDO (cresols and phenol) [51]. Thus, according to the DRIFTS data, the reaction products are absorbed on the surface of the catalysts, which is also confirmed by the XPS in the C 1 s and O 1 s regions.

The Raman spectra of MoO_x and WO_x is presented in Figure S9. According to the results of Raman spectroscopy, MoO_x represents crystalline MoO_3. The Raman bands at 995, 820, 670, 289 cm^{-1} are attributed to the Mo = O bond and the band at 210 cm^{-1} corresponds to the Mo–O–Mo bond. According to the XRD, the sample of MoO_x obtained at 360 °C is amorphous, which does not match with the results of Raman spectroscopy. Ajito et al. demonstrated that amorphous MoO_3 can be crystallized by the laser used to obtain the Raman spectrum [54]. There are two intense peaks in the Raman spectra of WO_x. The G peak at 1500–1600 cm^{-1} refers to the C–C bond, which is assigned to sp^2 hybridized carbon atoms, and the D peak at 1330–1390 cm^{-1}, which refers to the C–C bond (sp^3 hybridized carbon atoms). The presence of these peaks is associated with the adsorption of reaction products on the WO_x surface [55]. The peaks at 790, 700 and 250 cm^{-1} are broad, blurry and non-intense and refer to amorphous WO_3. However, according to the XRD, this catalyst has the crystal structure of $W_{18}O_{49}$. These differences can be explained by the low stability of $W_{18}O_{49}$. Lu et al. noted that $W_{18}O_{49}$ can be transformed into WO_3 by the laser used to carry out the Raman spectra [38].

2.2. Catalytic Activity

2.2.1. The Effect of Temperature in Toluene

The activity of catalysts obtained in situ was investigated in the HDO of guaiacol. The effect of temperature on the catalytic activity was evaluated over a wide temperature range of 120–380 °C, under an initial H_2 pressure of 5 MPa. The reaction time was 6 h, and toluene was used as a solvent. The conversion of guaiacol over MoO_x was noted to be extremely low and reached 1–4% at 120–200 °C (Figure S10a). A rise in temperature from 200 to 240 °C promoted a sharp increase in guaiacol conversion from 4 to 18%—which may be related to the full precursor transformation to oxides—the partial reduction of the catalyst, and, as a result, an increase in the number of oxygen vacancies. As shown in Figure 5a, the full conversion of guaiacol was reached at 320 °C. At 240–300 °C, phenol was observed as a main reaction product (Figure 5b). Anisole, cresols, and cyclohexene were also obtained. Since the bond dissociation energy of C_{AR}-OCH_3 is 45 kJ/mol and lower than that of the C_{Ar}–OH bond, the conversion of guaiacol to phenol was more favored than conversion to anisole [56]. The highest selectivity for phenol was 66% at 280 °C. A following temperature increase led to direct deoxygenation (DDO) of phenol to benzene. Therefore, the cleavage of the C_{Ar}–OH bond was favored at higher temperatures [11]. In this way, the selectivity for benzene gradually increased with a rise in temperature from 280 to 380 °C. Cyclohexane and xylenes were also detected in large amounts at 320–380 °C.

At 120–220 °C, guaiacol conversion over WO_x was very low and reached 1–5% (Figure S10b). The full conversion of guaiacol was reached at 360 °C (Figure 5c). Phenol was a major product at 240–300 °C. The decrease in phenol selectivity with a temperature increase from 240 °C to 380 °C is associated with its conversion to benzene (Figure 5d). Compared to MoO_x, WO_x demonstrated low catalytic activity in the hydrogenation of benzene to cyclohexene and cyclohexane. Oxygen vacancies in metal oxides are noted to act as active sites in hydrogenation reactions under typical HDO conditions [16,57]. With the temperature increase from 240 to 360 °C the selectivity for xylenes increased from 11 to 52%. As is the case with MoO_x, anisole was not detected among the reaction products at 320–380 °C. Most likely, it is caused by the conversion of anisole to phenol or cresols.

Phenol was the major product of guaiacol HDO at 240–300 °C over both catalysts. With a temperature increase to 320–340 °C, phenol selectivity over MoO_x decreased, and cyclohexane became the main product. In the case of WO_x, phenol was also obtained in significant amounts at 320–340 °C. However, xylenes formed with higher selectivity. With

a further increase in temperature to 360–380 °C, aromatics, such as benzene and xylenes, were obtained in large amounts over both catalysts. At this temperature, WO_x is more selective to aromatics than MoO_x.

The comparison of catalyst activities in the formation of HDO products (benzene, xylenes, cyclohexene, cyclohexane) is presented in Figure S11. The highest yield of HDO products (96%) was shown to be reached at 360 °C using MoO_x. Compared to MoO_x, the highest yield of HDO products over WO_x was 94% and was reached at 380 °C.

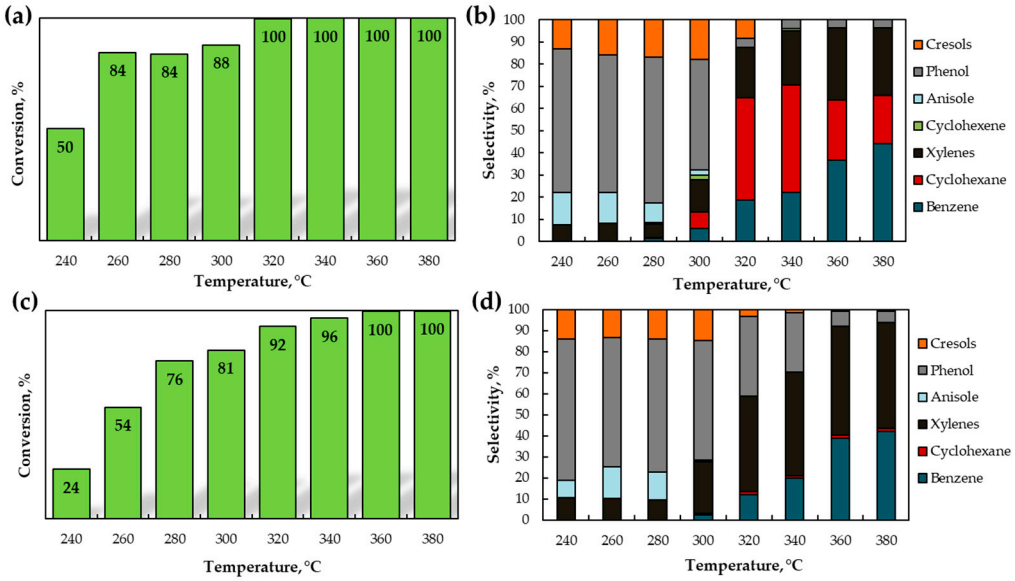

Figure 5. The results of guaiacol HDO over in situ-formed (**a**,**b**) MoO_x (**c**,**d**) WO_x. Reaction conditions: 120–380 °C, 5 MPa H_2, 6 h; 10 wt. % guaiacol in toluene solution.

2.2.2. The Effect of Pressure in Toluene

Because cyclohexane was formed in significant amounts when MoO_x was used as a catalyst, the effect of H_2 pressure (1–5 MPa) on product formation was studied (Figure 6). Guaiacol conversion was 100% in all cases. In the case of MoO_x, benzene, xylenes, cyclohexane and phenol were formed as products (Figure 6a). An increase in pressure led to a decrease in selectivity for benzene and an increase in selectivity for cyclohexane. Thus, carrying out the HDO of guaiacol over MoO_x under low H_2 pressure contributes to higher benzene selectivity. At the same time, H_2 pressure is shown to have almost no effect on benzene selectivity when WO_x is used as a catalyst (Figure 6b).

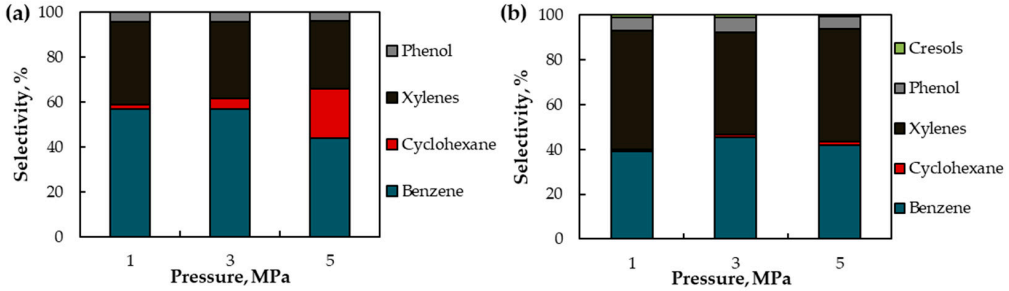

Figure 6. The results of guaiacol HDO over in situ formed (**a**) MoO_x (**b**) WO_x. Reaction conditions: 380 °C, 1–5 MPa H_2, 6 h; 10 wt. % guaiacol in toluene solution.

2.2.3. Reaction Pathways

The HDO of guaiacol over MoO_x and WO_x can occur via three routes, i.e., direct deoxygenation to anisole (DDO), demethoxylation to phenol (DMO), and DMO followed by methylation to cresols (Figure 7). The formation of cresols also occurs through transalky-

lation (TRA) of anisole [58]. Cresols can then convert to xylenes via two pathways: methylation (ME) to xylenols followed by DDO, or DDO to toluene followed by ME. However, xylenols were not detected, and toluene was used as a solvent. Phenol is formed not only by DMO of guaiacol but also by demethylation (DME) of anisole. Phenol then converts to benzene through DDO. Benzene is transformed into cyclohexene and cyclohexane by hydrogenation (HYD). Cyclohexene may also be formed by dehydratation of cyclohexanol, however, cyclohexanol was not identified in the reaction medium. Cyclohexane is also obtained by the HYD of cyclohexene.

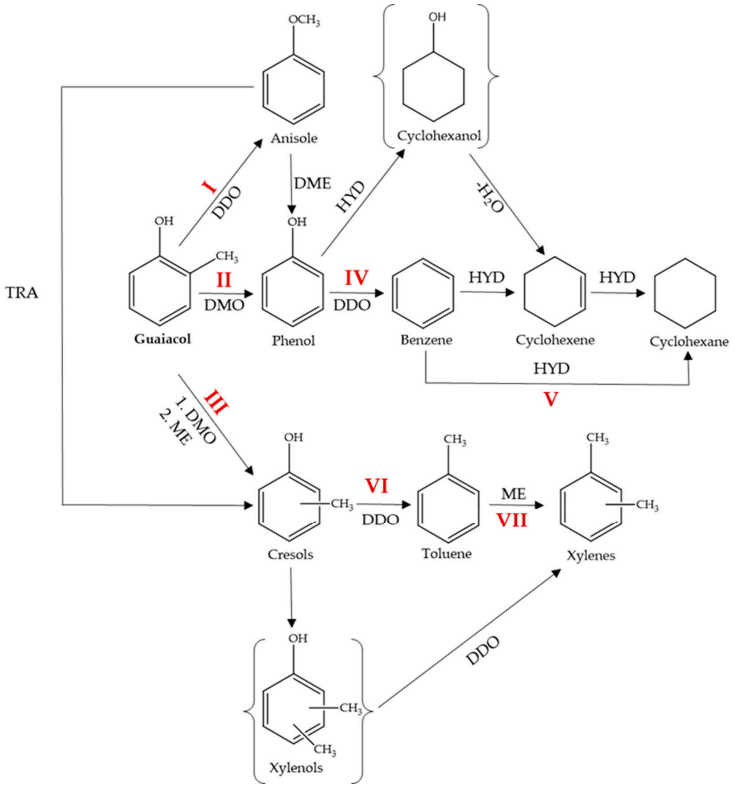

Figure 7. Proposed reaction pathways of guaiacol HDO over in situ formed MoO_x and WO_x. DDO—direct deoxygenation, HYD—hydrogenation, DMO—demethoxylation, DME—demethylation, ME—methylation, TRA—transalkylation. The following conditions favored each path: **I**—MoO_x or WO_x, 240–280 °C, 5 MPa (anisole is a minor product); **II**—MoO_x or WO_x, 240–300 °C, 5 MPa; **III**—MoO_x or WO_x, 240–300 °C, 5 MPa (cresols are minor products); **IV**—MoO_x, 320–360 °C, 5 MPa; 380 °C, 1–5 MPa; WO_x, 360 °C, 5 MPa; 380 °C, 1–5 MPa; **V**—MoO_x, 320–380 °C, 5 MPa; MoO_x, 340 °C, 5 MPa, 6 h; **VI, VII**—MoO_x or WO_x, 320–360 °C, 5 MPa; 380 °C, 1–5 MPa.

2.2.4. The Effect of Temperature and Pressure in Dodecane

Since xylenes were one of the reaction products, toluene was also probably formed. Thereby, the solvent was changed from toluene to dodecane. The catalytic tests were carried out at 300–380 °C, 5 MPa H_2, and 6 h of reaction. The yield of HDO products (benzene, toluene, xylenes, cyclohexene, cyclohexane) and the BTX fraction for both catalysts are shown in Figure 8. For both catalysts, the rise in the reaction temperature contributes to an increase in the yield of HDO products and the BTX fraction. At the same time, WO_x is more selective in the formation of BTX fraction, while in the presence of MoO_x, cyclohexane is also one of the HDO products. In addition, the catalytic tests were carried out at 380 °C, 1–5 MPa H_2 and 6 h of reaction. As shown in Figure S12, the selectivity for BTX products changes insignificantly, however, higher pressure results in more cyclohexane selectivity, especially when MoO_x is used.

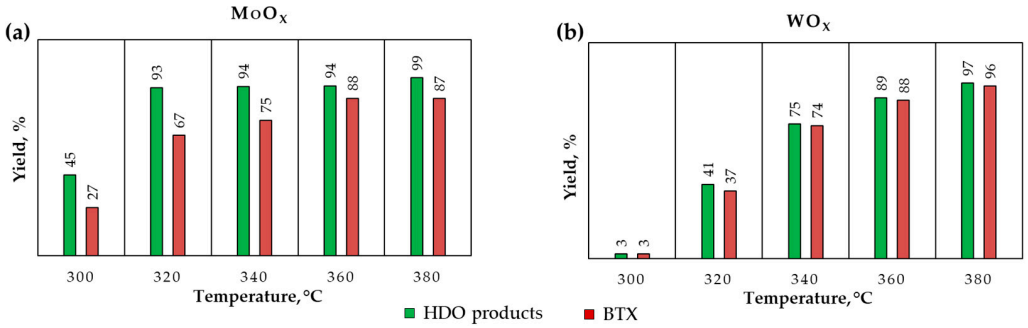

Figure 8. The yield of HDO products and BTX over in situ-formed (**a**) MoO_x (**b**) WO_x. Reaction conditions: 300–380 °C, 5 MPa H_2, 6 h; 10 wt. % guaiacol in dodecane solution.

2.2.5. The Recycling Tests

Five runs of recycling tests were carried out to estimate the stability of MoO_x and WO_x catalysts (Figure S13). The stability tests were carried out at average conversions (320 °C, 5 MPa H_2, 1 h). The conversion of guaiacol over MoO_x was 73% at the first run. It gradually decreased and was 56% after the fifth run. Such a decrease in conversion indicates insignificant deactivation of the MoO_x catalyst during the recycling test runs. Phenol and HDO product selectivity remained almost unchanged. At the same conditions, the conversion of guaiacol over WO_x changed significantly from 43% at the first run to 8% at the fifth run. The reason for this may be the adsorption on the catalyst surface of significant amounts of reaction products (confirmed by DRIFTS and Raman spectroscopy), and, as a consequence, the blocking of active sites. Phenol and HDO product selectivity changed insignificantly.

3. Materials and Methods

3.1. Materials

All reagents were purchased from commercial suppliers and used as received. Molybdenum hexacarbonyl (LLC "Redkino experimental plant," Redkino, Russia, wt. % of Mo 36.5–37.5%), and tungsten hexacarbonyl (LLC "Redkino experimental plant," Redkino, Russia, wt. % of W 51–52%) were used as precursors for catalyst preparation. Guaiacol (Acros organics, Geel, Belgium, >99%) was used as a substrate for hydrodeoxygenation. Toluene (Component-reaktiv, Moscow, Russia, >98.5%) or dodecane (Sigma-Aldrich, Burlington, VT, USA, >99%) were used as solvents. Acetone (Component-reaktiv, Moscow, Russia, >99.5%,) and petroleum ether 40/70 (Component-reaktiv, Moscow, Russia, tech.) were used for catalyst washing. H_2 (≥98%, Air Liquide, Paris, France) and Ar (≥98%, Air Liquide, Paris, France) gases were also used.

3.2. Catalyst Preparation and Catalytic Tests

The catalysts were prepared in a 45 mL stainless-steel batch autoclave reactor during the HDO of guaiacol. A mixture of 84.4 mg $Mo(CO)_6$ (or 113.7 mg $W(CO)_6$) and guaiacol (2 g of 10 wt. % solution in toluene or dodecane) was added to the reactor. The HDO of guaiacol was investigated at 120–400 °C for 6 h while undergoing constant magnetic stirring (7000 rpm). The initial pressure of H_2 was 5 MPa. After the catalytic test, the reactor was cooled to a room temperature. Liquid products were isolated from the reactor and separated from the catalysts by centrifugation (5000× *g* rpm). Catalysts obtained during the reaction were washed by petroleum ether and acetone until the solution over the catalysts became colorless. Then, the catalysts were dried in an argon atmosphere at room temperature.

3.3. Characterization

Powder X-ray diffraction was used to determine the phase composition of the catalysts. The X-ray diffractograms were obtained for a range of 5−100° 2θ by using a Rigaku Rotaflex

RU-200 diffractometer (CuK_α radiation) equipped with a Rigaku D/Max-RC goniometer (a rotation speed of 1°/min; a step 0.04°). Qualitative phase analysis of the samples was carried out using the PDF-2 ICDD database of powder diffraction patterns. The average crystallite sizes were estimated using the Scherrer equation.

X-ray photoelectron spectra were obtained using a PREVAC EA15 electronic spectrometer (AlK_α radiation, hν = 1486.74 eV, 150 W). Spectra were recorded at a pressure not exceeding 5×10^{-9} mbar. Spectra deconvolution was carried out using a PeakFit software.

The morphology of the catalysts obtained was observed using scanning electron microscopy and high-resolution transmission electron microscopy. Scanning electron microscopy with energy-dispersive X-ray spectroscopy was performed using a Carl Zeiss NVision 40 microscope equipped with an Oxford Instruments X-Max EDX detector operated at 20 kV. High-resolution transmission electron microscopy with energy-dispersive X-ray spectroscopy were performed using a FEI Tecnai Osiris transmission electron microscope equipped with a field emission electron gun operated at 200 kV.

Diffuse reflectance infrared Fourier transform spectroscopy was carried out in a high-temperature PIKE Diffus IR cell coupled with a VERTEX-70 Bruker Fourier transform IR spectrometer. DRIFT spectra of catalysts (194 scans at a resolution of 2 cm^{-1} in a range of 600–4000 cm^{-1}) were investigated in an argon flow in a temperature range of 25–450 °C. Spectra processing was carried out using OPUS-7 software. Raman spectra were obtained using a Senterra II spectrometer (laser power is 0.25 mW, a wavelength is 532 nm; a magnification is 50×).

Liquid reaction products were identified by gas chromatography–mass spectrometry using a Thermo Scientific ISQ 7000 GC-MS system equipped with a Restek 5XI-17SIL MS CAP capillary column (30 m × 0.25 mm × 0.25 μm), with helium being used as a carrier gas. The quantitative analysis of liquid products was carried out using a Crystallux 4000 M gas chromatograph equipped with a flame ionization detector, an Optima-1 capillary column (25 m × 0.32 mm × 0.35 μm), with helium used as a carrier gas. Chromatograms were obtained and analyzed using a NetChromWin software. Guaiacol conversion (%), product selectivity (%), and yield of full HDO products (%) were calculated using the following equations:

$$Conversion\ of\ guaiacol\ (\%) = \frac{mole\ of\ substrate\ consumed}{initial\ mole\ of\ substrate} \times 100\%$$

$$Selectivity\ (\%) = \frac{mole\ of\ product\ formed}{\sum moles\ of\ all\ products} \times 100\%$$

$$Yield\ of\ full\ HDO\ products\ (\%) = \frac{\sum moles\ of\ full\ HDO\ products}{initial\ mole\ of\ substrate} \times 100\%$$

$$Yield\ of\ BTX\ fraction\ (\%) = \frac{\sum moles\ of\ BTX}{initial\ mole\ of\ substrate} \times 100\%$$

4. Conclusions

Th possibility of obtaining in situ MoO_x and WO_x from the corresponding carbonyls during the HDO of guaiacol is shown in this study. According to XRD, MoO_x is amorphous, while WO_x displayed the crystalline patterns of WO_3 at 180 °C and $W_{18}O_{49}$ at 240–360 °C. The HRTEM of the catalysts obtained at 360 °C confirms the results of the XRD. It was shown via XPS that an increase in reaction temperature promoted the reduction of the surface M^{6+} to M^{4+}. In the case of MoO_x, the reduction proceeded through the formation of an intermediate M^{5+}. The presence of M^{5+} and M^{4+} may indicate vacancy sites on the surface of the catalysts.

The catalysts obtained were investigated in the HDO of guaiacol. Low guaiacol conversions at temperatures of 120–180 °C were associated with incomplete decomposition of the precursors. The active phase of the catalysts began to form at temperatures above 200 °C. An increase in the reaction temperature promoted the formation of vacancy sites

on which hydrodeoxygenation could proceed. The full conversion of guaiacol was reached at 320 °C (5 MPa, 6 h) and 360 °C (5 MPa, 6 h) using MoO_x and WO_x, respectively. MoO_x, compared to WO_x, is shown to demonstrate higher activity in the full HDO of guaiacol. However, WO_x is more selective in the production of aromatics, in particular the BTX fraction. The highest yield of the BTX was 96% (380 °C, 5 MPa, 6 h) using the WO_x catalyst.

Supplementary Materials: The following supporting information can be downloaded at: https://www.mdpi.com/article/10.3390/catal13020263/s1, Figure S1: X-ray diffractograms of (**a**) molybdenum and (**b**) tungsten carbonyls—the precursors of the catalysts; Table S1: Oxidation states (Mo 3d, W 4f regions) on the surface of the catalysts, identified by the XPS; Figure S2: The XPS spectra in C 1 s region of the catalysts obtained at different temperatures; Figure S3: The XPS spectra in O 1 s region of the catalysts obtained at different temperatures; Table S2: Oxidation states (C 1 s region) on the surface of the catalysts, identified by the XPS; Table S3: Oxidation states (O 1 s region) on the surface of the catalysts, identified by the XPS; Figure S4: The elemental mapping of MoO_x. Maps are assigned to (**a**) molybdenum, (**b**) oxygen, (**c**) molybdenum and oxygen, and (**d**) the HAADF image; Figure S5: The elemental mapping of WO_x. Maps are assigned to (**a**) tungsten, (**b**) oxygen, (**c**) tungsten and oxygen, and (**d**) the HAADF image; Figure S6: The EDX spectra of the catalysts: (**a**) MoO_x (**b**) WO_x; Figure S7: The DRIFT spectra of MoO_x in a range of 4000–600 cm^{-1}; Figure S8: The DRIFT spectra of WO_x in a range of 4000–600 cm^{-1}; Figure S9: The Raman spectra of MoO_x and WO_x; Figure S10: The results of the guaiacol HDO over in situ formed (**a**) MoO_x (**b**) WO_x. Reaction conditions: 120–220 °C, 5 MPa H_2, 6 h; 10 wt. % guaiacol in toluene solution; Figure S11: The yield of HDO products over in situ-formed MoO_x and WO_x. Reaction conditions: 240–380 °C, 5 MPa H_2, 6 h; 10 wt. % guaiacol in toluene solution.; Figure S12: The results of guaiacol HDO over in situ formed (**a**) MoO_x (**b**) WO_x. Reaction conditions: 380 °C, 1–5 MPa H_2, 6 h; 10 wt. % guaiacol in dodecane solution.; Figure S13: The recycling test runs of (**a**) MoO_x (**b**) WO_x. Reaction conditions: 320 °C, 5 MPa H_2, 1 h; 10 wt. % guaiacol in dodecane solution.

Author Contributions: Conceptualization, M.M., M.G. and A.M.; validation, M.M. and M.G.; formal analysis, M.M. and M.G.; investigation, M.M. and A.S.; resources, A.S.; writing—original draft preparation, M.M. and M.G.; writing—review and editing, M.G. and A.M.; visualization, M.M. and M.G.; supervision, M.G. and A.M.; project administration, M.G. and A.M. All authors have read and agreed to the published version of the manuscript.

Funding: This work was carried out within the State Program of TIPS RAS.

Data Availability Statement: Not applicable.

Acknowledgments: The authors thank Ivan Levin from TIPS RAS for the XRD analysis, Olga Arapova from TIPS RAS for the Raman spectroscopy and DRIFTs analysis, and Yury Grigoriev from A.V. Shubnikov Institute of Crystallography RAS for the HRTEM analysis. This work was performed using the equipment of the Shared Research Center Analytical center of deep oil processing and petrochemistry of the A.V. Topchiev Institute of Petrochemical Synthesis RAS and the JRC PMR IGIC RAS.

Conflicts of Interest: The authors declare no conflict of interest.

References

1. Nanda, S.; Mohammad, J.; Reddy, S.N.; Kozinski, J.A.; Dalai, A.K. Pathways of lignocellulosic biomass conversion to renewable fuels. *Biomass Convers. Biorefin.* **2014**, *4*, 157–191. [CrossRef]
2. Cherubini, F.; Strømman, A.H. Production of Biofuels and Biochemicals from Lignocellulosic Biomass: Estimation of Maximum Theoretical Yields and Efficiencies Using Matrix Algebra. *Energy Fuels* **2010**, *24*, 2657–2666. [CrossRef]
3. Tribot, A.; Amer, G.; Abdou, A.M.; de Baynast, H.; Delattre, C.; Pons, A.; Mathias, J.; Callois, J.; Vial, C.; Michaud, P.; et al. Wood-lignin: Supply, extraction processes and use as bio-based material. *Eur. Polym. J.* **2019**, *112*, 228–240.
4. Zhang, J.; Sun, J.; Wang, Y. Recent Advances in Selectively Catalytic Hydrodeoxygenation of Lignin-derived Oxygenates to Arenes. *Green Chem.* **2020**, *22*, 1072–1098. [CrossRef]
5. Führer, M.; Van Haasterechta, T.; Bitter, J.H. Cinnamaldehyde hydrogenation over carbon supported molybdenum and tungsten carbide catalysts. *Chem. Commun.* **2022**, *58*, 13608–13611. [CrossRef]
6. Yang, Y.; Liu, X.; Xu, Y.; Gao, X.; Dai, Y.; Tang, Y. Palladium-Incorporated α-MoC Mesoporous Composites for Enhanced Direct Hydrodeoxygenation of Anisole. *Catalysts* **2021**, *11*, 370. [CrossRef]

7. Kurisingal, J.F.; Lee, S.; Lee, J.G.; An, K. Zeolitic Imidazolate Framework Decorated Molybdenum Carbide Catalysts for Hydrodeoxygenation of Guaiacol to Phenol. *Catalysts* **2022**, *12*, 1605. [CrossRef]
8. Wang, F.; Wen, C.; Lu, M.; Zhang, P.; Zhu, J.; Li, M.; Shan, Y.; Song, C. SBA-15-supported ultrastable Mo_2N@CN catalysts for hydrodeoxygenation of guaiacol. *Biomass Bioenergy* **2023**, *168*, 106680. [CrossRef]
9. Golubeva, M.A.; Mukhtarova, M.; Bugaev, A.L.; Naranov, E.R. In Situ Generated Dispersed Catalysts Based on Molybdenum and Tungsten Phosphides in Hydroprocessing of Guaiacol. *Pet. Chem.* **2023**. [CrossRef]
10. Golubeva, M.A.; Mukhtarova, M.; Sadovnikov, A.A.; Maximov, A.L. Bulk Molybdenum and Tungsten Phosphides for Selective Phenol Production from Guaiacol. *ACS Omega* **2022**, *7*, 40586–40595. [CrossRef]
11. Zhang, X.; Tang, J.; Zhang, Q.; Liu, Q.; Li, Y.; Chen, L.; Wang, C.; Ma, L. Hydrodeoxygenation of lignin-derived phenolic compounds into aromatic hydrocarbons under low hydrogen pressure using Molybdenum oxide as catalyst. *Catal. Today* **2019**, *319*, 41–47. [CrossRef]
12. Jiang, S.; Ji, N.; Diao, X.; Li, H.; Rong, Y.; Lei, Y.; Yu, Z. Vacancy Engineering in Transition Metal Sulfide and Oxide Catalysts for Hydrodeoxygenation of Lignin-Derived Oxygenates. *ChemSusChem* **2021**, *14*, 4377–4396. [CrossRef] [PubMed]
13. Prasomsri, T.; Nimmanwudipong, T.; Román-Leshkov, Y. Effective hydrodeoxygenation of biomass-derived oxygenates into unsaturated hydrocarbons by MoO_3 using low H_2 pressures. *Energy Environ. Sci.* **2013**, *6*, 1732. [CrossRef]
14. Bagnato, G.; Sanna, A.; Paone, E.; Catizzone, E. Recent catalytic advances in hydrotreatment processes of pyrolysis bio-oil. *Catalysts* **2021**, *11*, 157. [CrossRef]
15. Thibodeau, T.J.; Canney, A.S.; DeSisto, W.J.; Wheeler, M.C.; Amar, F.G.; Frederick, B.G. Composition of tungsten oxide bronzes active for Hydrodeoxygenation. *Appl. Catal. A* **2010**, *388*, 86–95. [CrossRef]
16. Whiffen, V.M.L.; Smith, K.J. Hydrodeoxygenation of 4-Methylphenol over Unsupported MoP, MoS_2 and MoO_x Catalysts. *Energy Fuels* **2010**, *24*, 4728–4737. [CrossRef]
17. Wang, C.; Mironenko, A.V.; Raizada, A.; Chen, T.; Mao, X.; Padmanabhan, A.; Vlachos, D.G.; Gorte, R.J.; Vohs, J.M. Mechanistic Study of the Direct Hydrodeoxygenation of m-Cresol over WO_x-Decorated Pt/C Catalysts. *ACS Catal.* **2018**, *8*, 7749–7759. [CrossRef]
18. Wang, C.; Wittreich, G.R.; Lin, C.; Huang, R.; Vlachos, D.G.; Gorte, R.J. Hydrodeoxygenation of m-Cresol Over Pt-WO_x/C Using H_2 Generated In Situ by n-Hexane Dehydrogenation. *Catal. Lett.* **2020**, *150*, 913–921. [CrossRef]
19. Chen, T.; Kwon, O.; Huang, R.; Lin, C.; Vohs, J.M. WO_x promoted nickel catalyst for hydrodeoxygenation of m-cresol. *J. Catal.* **2021**, *400*, 294–300. [CrossRef]
20. Golubeva, M.A.; Maximov, A.L. Hydroprocessing of furfural over in situ generated nickel phosphide based catalysts in different solvents. *Appl. Catal. A* **2020**, *608*, 117890. [CrossRef]
21. Golubeva, M.A.; Maximov, A.L. Investigations on the Formation of Transition Metal Phosphides during the Hydrotreating of Light Cycle Oil Russ. *J. Appl. Chem.* **2021**, *94*, 1536–1545.
22. Vagvala, T.C.; Pandey, S.S.; Ogomi, Y.; Ma, T.; Hayase, S. Investigation of metal xanthates as latent curing catalysts for epoxy resin via formation of in-situ metal sulfides. *Inorg. Chim. Acta* **2015**, *435*, 292–298. [CrossRef]
23. Vutolkina, A.V.; Baygildin, I.G.; Glotov, A.P.; Cherednichenko, K.A.; Maksimov, A.L.; Karakhanov, E.A. Dispersed Ni-Mo sulfide catalysts from water-soluble precursors for HDS of BT and DBT via in situ produced H_2 under Water gas shift conditions. *Appl. Catal. B* **2021**, *282*, 119616. [CrossRef]
24. Kuchinskaya, T.; Kniazeva, M.; Samoilov, V.; Maximov, A. In Situ Generated Nanosized Sulfide Ni-W Catalysts Based on Zeolite for the Hydrocracking of the Pyrolysis Fuel Oil into the BTX Fraction. *Catalysts* **2020**, *10*, 1152. [CrossRef]
25. Zhang, K.; McCleese, C.; Lin, P.; Chen, X.; Morales, M.; Cao, W.; Seo, F.J.; Burda, C.; Baumgart, H. Synthesis of ALD Tungsten Trioxide Thin Films from $W(CO)_6$ and H_2O Precursors. *ECS Trans.* **2015**, *69*, 199–209. [CrossRef]
26. Davazoglou, D.; Moutsakis, A.; Valamontes, V.; Psychorish, V. Tungsten Oxide Thin Films Chemically Vapor Deposited at Low Pressure by $W(CO)_6$ Pyrolysis. *J. Electrochem. Soc.* **1997**, *144*, 595–599. [CrossRef]
27. Suvanto, M.; Pakkanen, T. Deposition of tungsten hexacarbonyl on alumina: A diffuse reflectance infrared Fourier transform spectroscopy study. *J. Mol. Catal. A Chem.* **1999**, *138*, 211–220. [CrossRef]
28. Ou, N.C.; Su, X.; Bock, D.C.; McElwee-White, L. Precursors for chemical vapor deposition of tungsten oxide and molybdenum oxide. *Coord. Chem. Rev.* **2020**, *421*, 213459. [CrossRef]
29. Dhas, N.A.; Gedanken, A. Characterization of Sonochemically Prepared Unsupported and Silica-Supported Nanostructured Pentavalent Molybdenum Oxide. *J. Phys. Chem. B* **1997**, *101*, 9495–9503. [CrossRef]
30. Dimitrova, Z.; Gogova, D. On the structure, stress and optical properties of CVD tungsten oxide films. *Mater. Res. Bull.* **2005**, *40*, 333–340. [CrossRef]
31. Fu, J.; Liu, S.; Zheng, W.; Huang, R.; Wang, C.; Lawal, A.; Alexopoulos, K.; Liu, S.; Wang, Y.; Yu, K.; et al. Modulating the dynamics of Brønsted acid sites on $PtWO_x$ inverse catalyst. *Nat. Catal.* **2022**, *5*, 144–153. [CrossRef]
32. Fang, Z.; Jiao, S.; Kang, Y.; Pang, G.; Feng, S. Photothermal Conversion of $W_{18}O_{49}$ with a Tunable Oxidation State. *ChemistryOpen* **2017**, *6*, 261–265. [CrossRef] [PubMed]
33. Baltrusaitis, J.; Mendoza-Sanchez, B.; Fernandez, V.; Veenstra, R.; Dukstiene, N.; Roberts, A.; Fairley, N. Generalized molybdenum oxide surface chemical state XPS determination via informed amorphous sample model. *Appl. Surf. Sci.* **2015**, *326*, 151–161. [CrossRef]

34. Xie, F.; Choy, W.C.H.; Wang, C.; Li, X.; Zhang, S.; Hou, J. Low-Temperature Solution-Processed Hydrogen Molybdenum and Vanadium Bronzes for an Efficient Hole-Transport Layer in Organic Electronics. *Adv. Mater.* **2013**, *25*, 2051–2055. [CrossRef] [PubMed]
35. Kim, H.; Cook, J.B.; Lin, H.; Ko, J.S.; Tolbert, S.H.; Ozolins, V.; Dunn, B. Oxygen vacancies enhance pseudocapacitive charge storage properties of MoO_{3-x}. *Nat. Mater.* **2017**, *16*, 454–460. [CrossRef] [PubMed]
36. Apergi, S.; Koch, C.; Brocks, G.; Olthof, S.; Tao, S. Decomposition of Organic Perovskite Precursors on MoO_3: Role of Halogen and Surface Defects. *Appl. Mater. Interfaces* **2022**, *14*, 34208–34219. [CrossRef] [PubMed]
37. Choi, J.G.; Thompson, L.T. XPS study of as-prepared and reduced molybdenum oxides. *Appl. Surf. Sci.* **1996**, *93*, 143–149. [CrossRef]
38. Lu, D.Y.; Chen, J.; Zhou, J.; Deng, S.Z.; Xu, N.S.; Xu, J.B. Raman spectroscopic study of oxidation and phase transition in $W_{18}O_{49}$ nanowires. *J. Raman Spectrosc.* **2007**, *38*, 176–180. [CrossRef]
39. Katoh, M.; Takeda, Y. Chemical State Analysis of Tungsten and Tungsten Oxides Using an Electron Probe Microanalyzer. *Jpn. J. Appl. Phys.* **2004**, *43*, 7292–7295. [CrossRef]
40. Lin, Y.-S.; Lai, J.-Y.; Tsai, T.-H.; Chuang, P.-Y.; Chen, Y.-C. Effects of oxygen addition on electrochromic properties in low temperature plasma-enhanced chemical vapor deposition-synthesized MoO_xC_y thin films for flexible electrochromic devices. *Thin Solid Films* **2011**, *519*, 3875–3882. [CrossRef]
41. Światowska-Mrowiecka, J.; de Diesbach, S.; Maurice, V.; Zanna, S.; Klein, L.; Briand, E.; Vickridge, I.; Marcus, P. Li-Ion Intercalation in Thermal Oxide Thin Films of MoO_3 as Studied by XPS, RBS, and NRA. *J. Phys. Chem. C* **2008**, *112*, 11050–11058. [CrossRef]
42. Ghasempour, R.; Iraji, A. Hybrid multiwalled carbon nanotubes and trioxide tungsten nanoparticles for hydrogen gas sensing. *J. Phys. D Appl. Phys.* **2009**, *42*, 165105. [CrossRef]
43. Li, J.; Zhou, C.; Mu, J.; Yang, E.; Zhao, X. In situ synthesis of molybdenum carbide/N-doped carbon hybrids as an efficient hydrogen-evolution electrocatalyst. *RSC Adv.* **2018**, *8*, 17202–17208. [CrossRef] [PubMed]
44. Sajadi, M.; Ranjbar, M.; Rasuli, R. Two-step synthesis of Ag-decorated MoO_3 nanotubes, and the effect of hydrogen doping. *Appl. Surf. Sci.* **2020**, *527*, 146675. [CrossRef]
45. Vasilopoulou, M.; Soultati, A.; Georgiadou, D.G.; Stergiopoulos, T.; Palilis, L.C.; Kennou, S.; Stathopoulos, N.A.; Davazoglou, D.; Argitis, P. Hydrogenated under-stoichiometric tungsten oxide anode interlayers for efficient and stable organic photovoltaics. *J. Mater. Chem. A* **2014**, *2*, 1738. [CrossRef]
46. Wang, J.; Gao, Y.; You, Z.; Fan, J.; Zhang, J.; Wang, S.; Xu, J. Laser Induced Nano and Micro Structures of Molybdenum Surface Applied in Multistage Depressed Collector for Secondary Electron Suppression. *Appl. Sci.* **2019**, *9*, 4374. [CrossRef]
47. Feng, C.; Tang, L.; Deng, Y.; Wang, J.; Tang, W.; Liu, Y.; Chen, Z.; Yu, J.; Wang, J.; Liang, Q. Synthesis of branched WO_3@$W_{18}O_{49}$ homojunction with enhanced interfacial charge separation and full-spectrum photocatalytic performance. *Chem. Eng. J.* **2020**, *389*, 124474. [CrossRef]
48. Chen, C.L.; Mori, H. In situ TEM observation of the growth and decomposition of monoclinic $W_{18}O_{49}$ nanowires. *Nanotechnology* **2009**, *20*, 285604. [CrossRef]
49. Hahn, T.; Bentrup, U.; Armbrüster, M.; Kondratenko, E.V.; Linke, D. The Enhancing Effect of Brønsted Acidity of Supported MoO_x Species on their Activity and Selectivity in Ethylene/trans-2-Butene Metathesis. *ChemCatChem* **2014**, *6*, 1664–1672. [CrossRef]
50. Zafeiratos, S.; Papakonstantinou, G.; Jacksic, M.M.; Neophytides, S.G. The effect of Mo oxides and TiO_2 support on the chemisorption features of linearly adsorbed CO on Pt crystallites: An infrared and photoelectron spectroscopy study. *J. Catal.* **2005**, *232*, 127–136. [CrossRef]
51. Baes, A.U.; Bloom, P.R. Diffuse Reflectance and Transmission Fourier Transform Infrared (DRIFT) Spectroscopy of Humic and Fulvic Acids Soil. *Sci. Soc. Am. J.* **1989**, *53*, 695–700. [CrossRef]
52. Barreto, M.S.C.; Reis, J.V.; Muraoka, T.; Jemo, M.; Vergutz, L.; Alleoni, L.R.F. Diffuse reflectance infrared Fourier transform spectroscopy for a qualitative evaluation of plant leaf pigment extraction. *Analyst* **2021**, *146*, 3440. [CrossRef] [PubMed]
53. Li, C.; Zhang, C.; Zhang, L.; Gholizadeh, M.; Hu, X. Biochar catalyzing polymerization of the volatiles from pyrolysis of poplar wood. *Int. J. Energy. Res.* **2021**, *45*, 13936–13951. [CrossRef]
54. Ajito, K.; Nagahara, L.A.; Tryk, D.A.; Hashimoto, K.; Fujishima, A. Study of the Photochromic Properties of Amorphous MoO_3 Films Using Raman Microscopy. *J. Phys. Chem.* **1995**, *99*, 16383–16388. [CrossRef]
55. Casiraghi, C.; Piazza, F.; Ferrari, A.C.; Grambole, D.; Robertson, J. Bonding in hydrogenated diamond-like carbon by Raman spectroscopy. *Diamond Relat. Mater.* **2005**, *14*, 1098–1102. [CrossRef]
56. Tran, N.T.T.; Uemura, Y.; Chowdhury, S.; Ramli, A. Vapor-phase Hydrodeoxygenation of Guaiacol on Al−MCM−41 Supported Ni and Co Catalysts. *Appl. Catal. A* **2016**, *512*, 93–100. [CrossRef]
57. Bui, V.N.; Laurenti, D.; Afanasiev, P.; Geantet, C. Hydrodeoxygenation of guaiacol with CoMo catalysts. Part I: Promoting effect of cobalt on HDO selectivity and activity. *Appl. Catal. B* **2011**, *101*, 239–245. [CrossRef]
58. Venkatesan, K.; Krishna, J.V.J.; Anjana, S.; Selvam, P.; Vinu, R. Hydrodeoxygenation kinetics of syringol, guaiacol and phenol over H-ZSM-5. *Catal. Commun.* **2021**, *148*, 106164. [CrossRef]